JMEPEG (2016) 25:220–226
DOI: 10.1007/s11665-015-1811-8

Bending Fatigue of Carburized Steel at Very Long Lives

D.V. Nelson and Z. Long

(Submitted October 27, 2015; in revised form October 29, 2015; published online December 14, 2015)

The bending fatigue behavior of two carburized steels is investigated for lives between approximately 10^5 and 10^8 cycles. Cracks are observed to start at sub-surface inclusions and develop features on fracture surfaces resembling "fish eyes" in appearance. This type of sub-surface cracking tends to govern fatigue strength at long lives. Previous studies of "fish eye" fatigue in carburized steel have been relatively few and have mainly considered failures originating at depths beneath a carburized case, where compressive residual stresses are minimal and hardness values approach those in the core. This study provides fatigue data for cracks originating within cases at various depths where compressive residual stresses are substantial and hardness is much higher than in the core. Fatigue strength is predicted by a simple model, accounting for the influence of residual stresses and hardness values at the different depths at which cracks started. Predictions of fatigue strength are compared with data generated in this study.

Keywords carburizing, fish eye, heat treatment, high-cycle fatigue, life prediction, residual stress, steel

1. Introduction

Numerous mechanical components made of hardened steel are designed to have fatigue lives exceeding millions of cycles, a regime in which failures tend to originate at sub-surface inclusions (Ref 1). In that regime, a penny-shaped crack typically grows from an inclusion with a distinct appearance known as a "fish eye." An example is shown in Fig. 1. This type of fatigue failure has been the subject of increasing study during the past decade and is considered in a number of review articles (Ref 2-6). A zone of special interest surrounding an inclusion is often found within a fish eye. The zone is referred to as an optically dark area (ODA) (Ref 1) (or in some cases, a granular bright facet (Ref 7), fine granular area (Ref 3), or rough surface area (Ref 8)). ODAs are believed to start early in fatigue life (first 10% or so of life) and gradually increase in size, occupying most of the fatigue life (Ref 9, 10). Little life is typically spent in the growth of a crack from the ODA size to fracture (Ref 11). An example of an ODA is shown in Fig. 2.

To date, studies of "fish eye" fatigue have primarily used through-hardened specimens. Many mechanical components are case hardened, producing a profile in hardness and residual stresses as a function of depth below the surface. Carburizing is a widely used case-hardening process applied to gears, bearings, camshafts, etc. Not only does it alter sub-surface hardness and create residual stresses, but it also leads to hydrogen around internal non-metallic inclusions (Ref 12). In this study, the high-cycle fatigue behavior of carburized gear steels is explored to assess the influences of residual stresses and hardness on "fish eye" fatigue cracks occurring within carburized cases.

D.V. Nelson, Mechanical Engineering Department, Stanford University, Stanford, CA 94305; and **Z. Long**, Mechanical Engineering Department, Stanford University, Stanford, CA 94305; and Department of Mechanical & Vehicular Engineering, Beijing Institute of Technology, Beijing 100081. Contact e-mail: dnelson@stanford.edu.

A 1968 study by Funatani and Noda (Ref 13) on the bending fatigue of carburized specimens noted that fish eye cracks initiated at depths approximately equal to case depth, where compressive residual stresses were relatively minimal (less than −100 MPa) compared to bending stresses. Naito et al. (Ref 14) tested carburized specimens with either non-martensitic or electropolished surface layers. Surface failures originated in non-martensitic layers even at lives approaching 10^8 cycles (the highest number of cycles tested). In electropolished specimens, several fish eye failures at inclusions were noted for lives of about 5×10^6 cycles and greater, but sizes and depths of inclusions were not reported except in one photo where the depth was approximately 250 μm, within the carburized case. Murakami et al. (Ref 15) tested carbonitrided specimens with a case depth of approximately 2 mm. Fish eye cracks started at inclusions deeper than the case. Residual stresses versus depth within the case were not reported, which is understandable since cracks did not originate there. Huang et al. (Ref 16) tested carburized specimens with a relatively shallow case (approx. 0.3 mm). Depths of inclusions at which cracks formed and residual stresses versus depth were not mentioned.

This study differs from those just reviewed by reporting the results of fatigue tests in which fish eye cracks started within the cases of carburized specimens, at depths where magnitudes of compressive residual stresses were significant relative to applied stresses and where hardness values were much higher than in the core. To date, approaches for predicting "fish eye" fatigue strength have been developed largely using test data from specimens with minimal residual stresses and hardness nearly uniform with depth. This study provides an opportunity to assess the usefulness of a prominent approach for predicting fatigue strength for situations where failures may originate within the case, at depths where residual stresses are substantial and hardness values vary with depth.

2. Experimental Procedure

Two Cr-Ni carburized gear steels, 20Cr2Ni4 and 17Cr2Ni2, designated A and B, respectively, were tested. Table 1 shows their nominal chemical compositions and tensile properties. The geometry and nominal dimensions of a first set of fatigue specimens made of alloys A and B are shown in Fig. 3. Fatigue tests with the first set involved loading levels that unexpectedly caused ball bearings in a rotating bending fatigue test machine to fail prematurely. A second set of smaller specimens with a nominal diameter of 5.6 mm allowed additional testing at lower load levels, avoiding further bearing failures. The second set is designated NA, NB. Both sets of specimens were carburized at 910 °C for 20 h with a carbon potential of 1.2% and then air-cooled and held at 650 °C for 2 h. After that, the specimens were austenitized at 880 °C for 2 h, oil quenched, and tempered at 180 °C for 2 h. After carburizing and hardening, specimens were gently ground and polished in the longitudinal direction with abrasive paper (to grade #2000) to achieve a mirror-like finish.

Carburized cases were etched with picric acid to reveal prior austenite grain boundaries. Applying ASTM E112-10 (Ref 17), the average grain size was determined to be G8.5 and G9 for steels A and B, respectively, or 19 and 16 μm. Micro-hardness profiles of carburized cases determined according to ASTM E384-10 (Ref 18) are reported in Fig. 4. Specimens made of alloy B developed a somewhat harder case. Longitudinal residual stresses versus depth were measured by x-ray diffraction using conventional Cr-Ka radiation (2.291A wavelength), [211] planes, and the $\sin^2\psi$ method combined with layer removal by electropolishing. Stresses were corrected for the effect of layer removal (Ref 19). Residual stresses measured in specimens that had been cycled without failure are shown in Fig. 5. Compressive residual stresses in representative specimens A and NA were larger than those in the corresponding B and NB specimens. In the second set of specimens (NA,NB) with a somewhat smaller diameter, significant residual stresses were present over shallower depths than in the first set. Magnitudes of residual stresses in Fig. 5 for depths greater than about 0.2 mm are comparable to typical values for carburizing in the range of −250 to −350 MPa (Ref 20), while values near the surface are in line with those approaching −800 MPa reported for carburized and ground gear teeth (Ref 21). The magnitudes of residual stresses measured suggest that little or no residual stress relaxation occurred from fatigue cycling. The yield strength near the surface of specimens was estimated to be approximately 2000 to 2100 MPa based on correlations between hardness and yield strength for carburized steel (Ref 22). With the exception of one specimen, the bending stress amplitude at the surface was 1150 MPa or less in the testing to be described shortly, so that the sum of applied and residual stresses would not be expected to cause significant relaxation of residual stresses by plastic deformation (Ref 23).

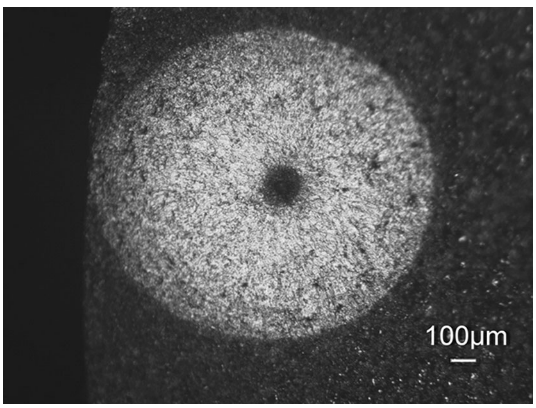

Fig. 1 Typical "fish eye" originating at a sub-surface inclusion in this study. (Specimen surface is shown to the left of the fish eye)

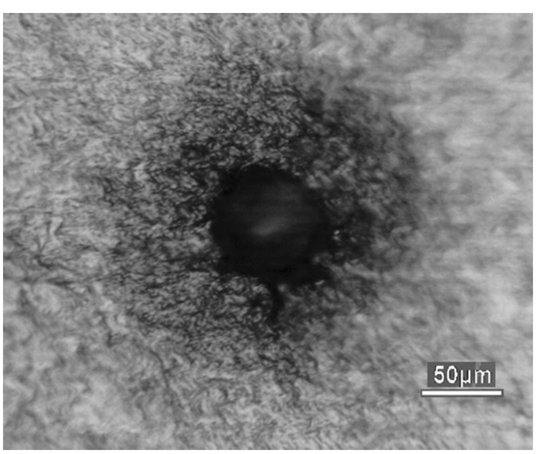

Fig. 2 Optically dark area surrounding an inclusion

3. Experimental Results

Fatigue tests were conducted at room temperature in air. The loading frequency was 75 Hz. The results of fatigue testing are

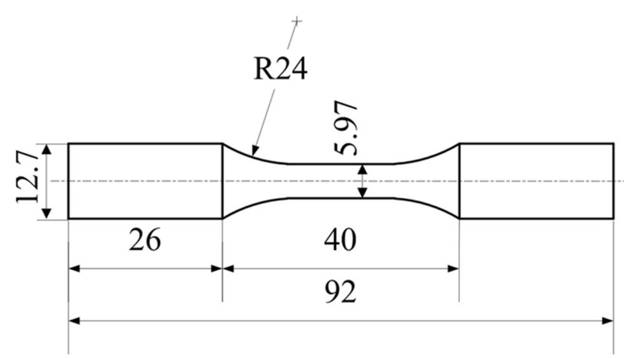

Fig. 3 Geometry of fatigue specimen (dimensions in mm)

Table 1 Chemical composition (wt.%) and tensile properties of the steels prior to carburizing

Alloy	C	Si	Mn	Cr	Ni	Mo	S_y, MPa	S_u, MPa	RA, %
A	0.17-0.23	0.17-0.37	0.3-0.6	1.25-1.65	3.25-3.65	0.1-0.1 5	1292	1483	57
B	0.14-0.19	0.17-0.37	0.3-0.6	1.5-1.8	1.4-1.7	0.25-0.35	1150	1400	35

S_y yield strength, S_u ultimate tensile strength, *RA* reduction of area

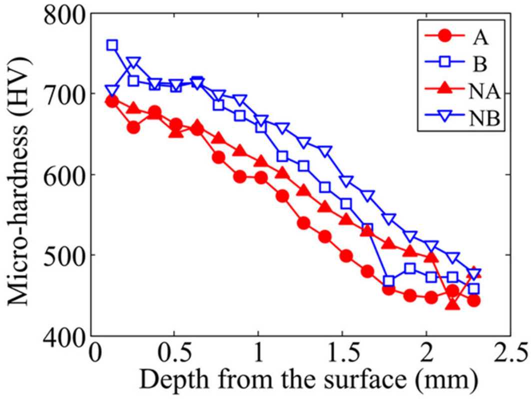

Fig. 4 Micro-hardness profiles

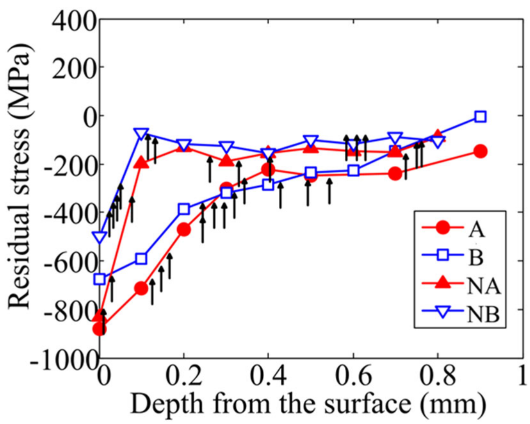

Fig. 5 Residual stress profiles, with arrows showing depths at which cracks started

shown in Fig. 6, where bending stress amplitude refers to values at the surface. The fracture surfaces of the failed specimens were examined by optical microscopy as well as with a scanning electron microscope (SEM) equipped with an x-ray energy-dispersive spectrometer (EDS). Based on the result of EDS, all internal fractures originated at non-metallic inclusions that were either Al_2O_3 or TiN. Sizes of inclusions in terms of a $\sqrt{\text{area}}$ parameter ranged between 16 and 49 μm, where *area* is the projected area of a defect or crack on a plane normal to the direction of maximum tensile stress (Ref 1). The $\sqrt{\text{area}}$ parameter will be used later in a model for fatigue strength. In the case of a circular area, the parameter $\sqrt{\text{area}} = 0.89 \times \text{diameter}$. Inclusions causing fish eye cracks were observed at depths ranging from 10 to 745 μm. ODAs could be identified at most crack initiation sites, with $\sqrt{\text{area}}$ values (including the area of the inclusion within an ODA) between 30 and 99 μm. Figure 7(a) shows an example of a fish eye fracture that initiated from an unbroken Al_2O_3 inclusion, while Fig. 7(b) shows a pore left by an inclusion debonded from the matrix, suggesting relatively weak bonding between the inclusion and matrix. Several radial ridges emanated from the crack origin. The length of these ridges ranged from 16 to 100 μm, and many of the short ridges stopped at the outer border of ODAs. Nishijima and Kanazawa (Ref 24) have suggested that such ridges indicate shear cracking similar to what might be found for cracks that initiate at a surface. The size of each ODA, normalized by the size of the corresponding

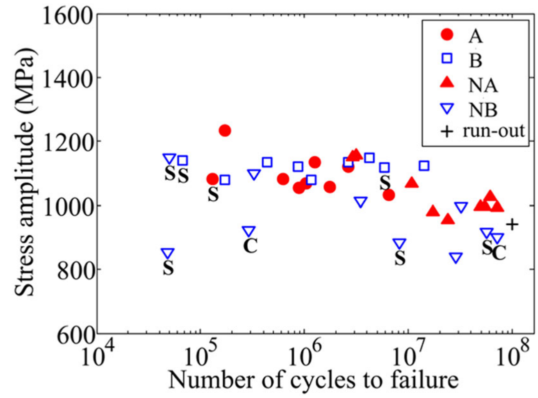

Fig. 6 Fully reversed bending fatigue data, with symbol S indicating cracking originating at the surface and C denoting a combination of surface cracking and sub-surface fish eye cracking

inclusion from which a fish eye crack started, is shown in Fig. 8. Although there is significant scatter, the ratio of ODA-to-inclusion size tends to increase at longer lives. Finally, it is of interest to note that one NB specimen tested at 850 MPa had an unexpectedly short life, as seen in Fig. 6. Examination of the fracture surface suggested that failure originated at a large surface inclusion, with no evidence of fish eye cracking.

Figure 5 shows depths of inclusions at which fish eye cracks formed relative to compressive residual stress versus depth. Most of the cracks started at locations with significant residual stress. There was no evidence of oxidation or decarburization at any of the locations where cracks started.

The fatigue strength, σ_w (MPa), of each specimen with a fish eye fracture was estimated by Murakami's $\sqrt{\text{area}}$ parameter model (Ref 1) given in Eq 1, which was derived from a fracture mechanics analysis along with data from specimens of uniform hardness and assumed minimal residual stress. The model has become prominent in evaluations of fatigue strength governed by cracking from inclusions:

$$\sigma_w = \frac{1.56\,(\text{Hv} + 120)[(1 - R)/2]^{\beta}}{\left(\sqrt{\text{area}_{\text{inc}}}\right)^{1/6}}, \tag{Eq 1}$$

where Hv is Vickers hardness, area_{inc} is the projected area (μm) of an inclusion normal to the direction of stress, R is the ratio of minimum to maximum stress in a cycle, and β is given by

$$\beta = 0.226 + 10^{-4}\,\text{Hv} \tag{Eq 2}$$

$$R = (\sigma_m - \sigma_w)/(\sigma_m + \sigma_w), \tag{Eq 3}$$

where σ_m is the mean value of applied stress.

Here, the influence of residual stresses σ_{res} is taken into account as if it was a mean stress σ_m in Eq 3. The bending stress amplitude σ_a at the sub-surface location of an inclusion was obtained from

$$\sigma_a = \sigma_{\text{nominal}}\left(1 - \frac{d_{\text{inc}}}{r_s}\right), \tag{Eq 4}$$

where σ_{nominal} is the bending stress amplitude at the surface, d_{inc} is the depth of an inclusion from the surface, and r_s is the measured radius of the minimum section of specimens. The values of hardness and residual stress measured at the depth of a given inclusion were used in Eq 1-3. Since σ_w is a function of R in Eq 1, and R is a function of σ_w in Eq 3, determination of both can start by taking $\sigma_w = \sigma_a$ to obtain an initial value of R, and then to find an updated value of σ_w, which is used to find an updated value of R, and so forth until convergence is obtained.

Figure 9(a) shows the relation between the ratio of the applied stress amplitude to the estimated fatigue strength, (σ_a/σ_w), and the number of cycles to failure, N_f. The ratio (σ_a/σ_w) is conservative, except where it drops slightly below unity approaching 10^8 cycles. The values of (σ_a/σ_w) provide evidence that Murakami's model in Eq 1 can also be effective for fatigue strength estimates of carburized and ground steel when fish eye cracks start at depths in carburized cases where compressive residual stresses are significant and fatigue lives are in the range of 10^5 to 10^8 cycles. The relation between (σ_a/σ_w) and the depth of inclusions is shown in Fig. 9(b). There is no apparent dependence of (σ_a/σ_w) on the depth. If desired, the use of $\sqrt{\mathrm{area}_{\mathrm{ODA}}}$ rather than $\sqrt{\mathrm{area}_{\mathrm{inc}}}$ in Eq 1 would provide lower, more conservative estimates of predicted fatigue strength σ_w (approximately 7% more conservative for the data here).

It has been proposed that there may be two kinds of crack growth thresholds for fish eye failures. A larger one, characterized by the stress intensity factor range ΔK at the outer border of ODAs, represents a threshold for a transition from small crack growth to "Paris law" behavior (Ref 25), and a smaller one, characterized by ΔK at the border of inclusions, represents a threshold for crack growth to occur from an inclusion (Ref 26). To account for the effect of compressive residual stress, the stress intensity factor range at the border of an inclusion, ΔK_{inc}, and at the outer border of an ODA, ΔK_{ODA}, was computed using an $\sqrt{\mathrm{area}}$ model (Ref 1) modified here to account for the effect of residual stresses:

$$\Delta K_{\mathrm{inc}} = 0.5\,(\sigma_a + \sigma_{res})\sqrt{\pi\sqrt{\mathrm{area}_{\mathrm{inc}}}} \quad \text{(Eq 5)}$$

$$\Delta K_{\mathrm{ODA}} = 0.5\,(\sigma_a + \sigma_{res})\sqrt{\pi\sqrt{\mathrm{area}_{\mathrm{ODA}}}}, \quad \text{(Eq 6)}$$

where $\sqrt{\mathrm{area}_{\mathrm{inc}}}$ and $\sqrt{\mathrm{area}_{\mathrm{ODA}}}$ are the projected areas of an inclusion and an ODA, respectively. The values of applied stress amplitude, σ_a, and residual stress, σ_{res}, were taken at the sub-surface location of a given inclusion. (Compressive σ_{res} has a negative sign in Eq 5 and 6).

Figure 10 shows ΔK_{inc} and ΔK_{ODA} values versus cycles to failure N_f. For the A specimens, ΔK_{inc} varies between 2.6 and 3.4 MPa$\sqrt{m}$ with an average of 3.0 MPa$\sqrt{m}$, while ΔK_{ODA} varies between 3.6 and 4.9 MPa$\sqrt{m}$ with an average of 4.3 MPa$\sqrt{m}$. For the NA specimens, ΔK_{inc} varies between 1.1 and 3.1 MPa$\sqrt{m}$ with an average of 2.3 MPa$\sqrt{m}$, while ΔK_{ODA} varies between 1.7 and 5.5 MPa$\sqrt{m}$ with an average of 4.5 MPa$\sqrt{m}$. For the B specimens, ΔK_{inc} varies between 2.3 and 3.9 MPa$\sqrt{m}$ with an average of 2.9 MPa$\sqrt{m}$, while ΔK_{ODA} varies between 3.8 and 5.4 MPa$\sqrt{m}$ with an average of 4.7 MPa$\sqrt{m}$. For the NB specimens, ΔK_{inc} varies between 2.9 and 3.8 MPa$\sqrt{m}$ with an average of 3.3 MPa$\sqrt{m}$, while ΔK_{ODA} varies between 4.2 and 4.9 MPa$\sqrt{m}$ with an average of 4.5 MPa$\sqrt{m}$. The average value of ΔK_{inc} for all of the specimens in this study was 2.9 MPa$\sqrt{m}$, while the average value of ΔK_{ODA} was 4.5 MPa$\sqrt{m}$. Those values, which were computed to account for the presence of significant residual stresses, compare well with the values in the range of ΔK_{inc} from 2 to 4 MPa$\sqrt{m}$ for steels with similar martensitic microstructures and hardness but *without* residual stresses from case hardening (Ref 26-35). The values of ΔK_{ODA} computed here fall in the range of 3-6 MPa$\sqrt{m}$ typically reported for such steels without residual stresses (Ref 26, 27, 30-37).

If residual and applied stresses versus depth within a carburized case are known, then ΔK_{inc} and ΔK_{ODA} can be computed as a function of depth for a range of inclusion sizes expected to assess the potential for fish eye failures. This could

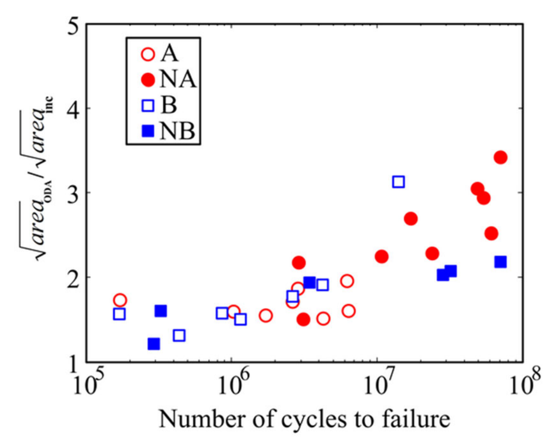

Fig. 8 Ratio of the size of an ODA to that of the inclusion from which fish eye cracking developed

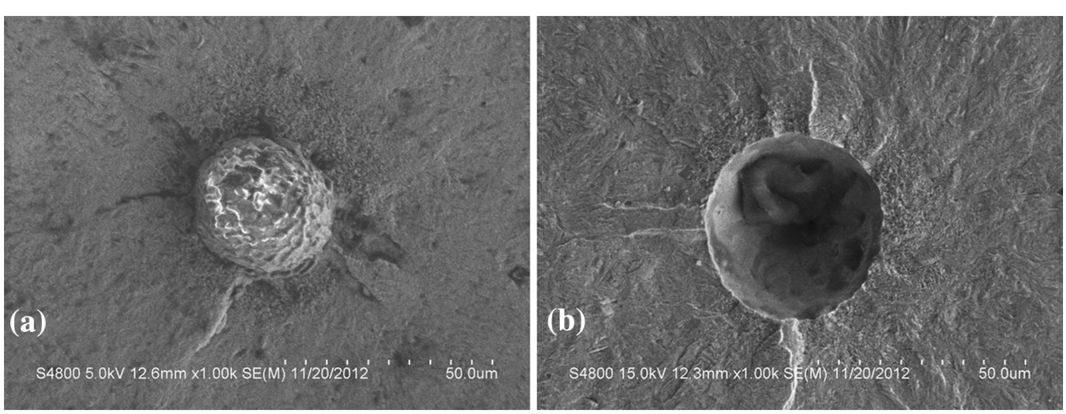

Fig. 7 (a) Inclusion at the center of a fish eye for a specimen of steel A, σ_a = 1041 MPa, N_f = 2,651,000 cycles, $\sqrt{\mathrm{area}}$ = 28 μm; (b) pore at the center of a fish eye for a specimen of steel B, σ_a = 1067 MPa, N_f = 1,149,800 cycles, $\sqrt{\mathrm{area}}$ = 35 μm

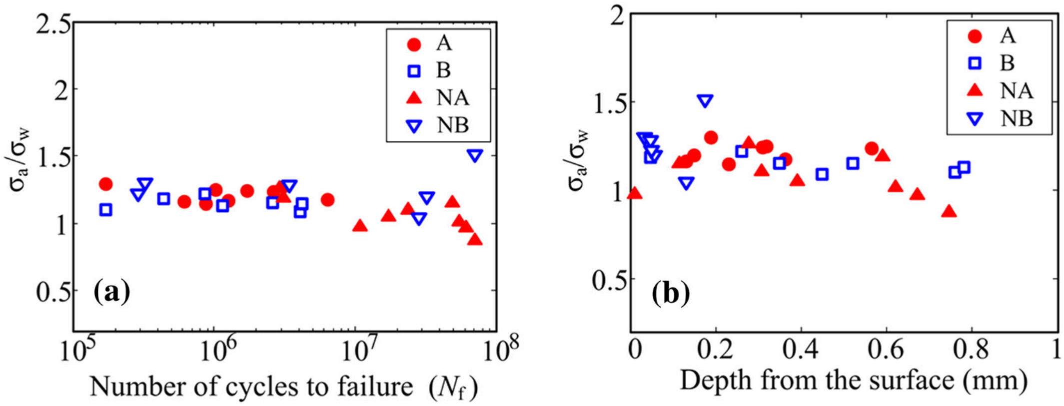

Fig. 9 Fish eye failures evaluated using Murakami's $\sqrt{area}$ model (Eq 1): ratio of applied stress amplitude to estimated fatigue strength vs. (a) cycles to failure and (b) depth of inclusions

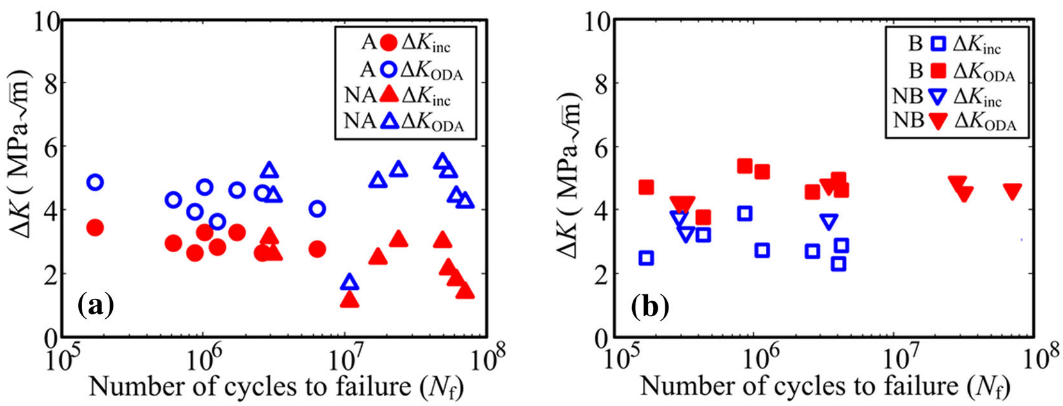

Fig. 10 Stress intensity factor range at inclusions and at ODAs vs. cycles to failure for (a) alloy A and (b) alloy B

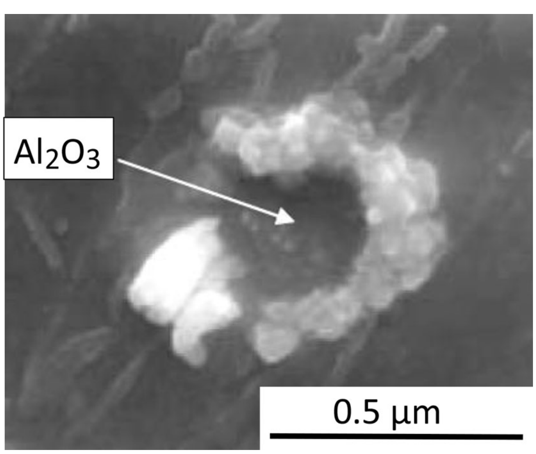

Fig. 11 Signature of hydrogen at an inclusion, observed by tritium microautoradiography. Image modified from (Ref 38) and © 2005 by the American Nuclear Society, LaGrange, Illinois

provide information useful for alloy selection, design analysis, and heat treatment. For instance, trade-offs between fish eye fatigue strength and inclusion sizes, applied stress levels, etc. could be explored.

4. Discussion

As noted in the introduction, most of the fatigue life associated with the fish eye phenomenon is believed to be spent in the formation of ODAs at inclusions. Different mechanisms have been suggested for the development of ODAs. Murakami et al. (Ref 15) suggested that hydrogen plays an important role in fish eye crack development, perhaps by embrittlement. Figure 11 shows an example of a "signature" of hydrogen trapped at an inclusion as observed by a specialized technique known as tritium automicroradiography (Ref 38). Shiozawa et al. (Ref 9, 39) proposed that ODAs are formed by carbide decohesion, growth of microcracks along boundaries between carbides and the matrix, plus microcrack coalescence. Hydrogen is known to have the potential to reduce cohesive strength at carbide-to-matrix interfaces (Ref 40), and it seems plausible that hydrogen may promote the mechanism suggested by Shiozawa et al. Sakai (Ref 3) suggested a mechanism for development of ODAs in which very fine sub-grains with different crystallographic orientations are formed by micro-scale polygonization and debonding, along with coalescence of the micro-debondings. Grad et al. (Ref 41) found that cyclic loading combined with the stress concentration created by inclusions caused significant grain refinement within ODAs. As Li (Ref 4) has noted, hydrogen-assisted local plasticity may promote dislocation activity and multi-slip around inclusions. That influence may, in turn, encourage mechanisms such as polygonization and grain refinement.

When it comes to the influence of hydrogen on the phenomenon of fish eye fatigue originating within carburized cases, relatively little appears to be known. Gas carburizing and direct hardening have been found to produce a substantial initial hydrogen content of about 2 ppm (Ref 42), while tempering at 200 °C in air for one hour in air resulted in approximately 50% hydrogen effusion. Tempering in vacuum caused 75% effusion in 30 min. Effusion during tempering in air was likely inhibited by an increasingly thick oxide layer (Ref 42). Empirical corrections to Eq 1 have been proposed (Ref 43, 44) to account for effects of hydrogen concentration on fatigue strength based on tests of small, through-hardened alloys. Similar relations for fish eye cracks originating within carburized cases remain to be explored. It may be of interest in future studies of fish eye fatigue to investigate how hydrogen content varies with depth within carburized cases using a measurement approach like that applied by Murakami and Matsunaga (Ref 45) to hydrogen-charged specimens of stainless steels. Carburized specimens with and without oxidized layers might be tested to see how hydrogen content and subsurface concentration versus depth differ.

5. Conclusions

1. Previous studies on fish eye fatigue in carburized specimens in which depths of crack origins were reported showed that origins were typically at depths where compressive residual was minimal and hardness values were close to those in the core. By contrast, most fish eye fatigue cracks started at sub-surface inclusions within the case of carburized specimens in this study, at depths where compressive residual stresses were significant and where hardness values were much higher than in the core.
2. Murakami's $\sqrt{\text{area}}$ parameter model was found to be effective in predicting fatigue strength by taking into account hardness and compressive residual stresses at the depths of inclusions from which fish eye cracks originated.
3. An average value of stress intensity factor range ΔK_{inc} at the border of inclusions, computed to account for residual stresses and applied stresses, was 2.9 $\text{MPa}\sqrt{m}$, comparable to values in the literature for specimens that had minimal residual stresses at locations where fish eye cracks originated. ΔK_{inc} can be considered a threshold for crack growth to occur from an inclusion. An average value of ΔK_{ODA} at the outer border of ODAs, also computed to account for residual stresses, was 4.5 $\text{MPa}\sqrt{m}$, again comparable to the values from specimens with minimal residual stresses. ΔK_{ODA} can be considered a threshold for a transition from small crack growth to "Paris law" behavior. The ability to account for the influence of residual stresses in determining ΔK_{inc} and ΔK_{ODA} by superposition of applied and residual stresses is supported by the data generated in this study.

Acknowledgments

We would like to acknowledge Technology for Energy Corp. for providing x-ray diffraction data and Anamet Labs for hardness measurements.

References

1. Y. Murakami, *Metal Fatigue: Effects of Small Defects and Nonmetallic Inclusions*, Elsevier Science Ltd., Oxford, 2002
2. M. Capetti, T. Tagawa, and T. Miyata, Ultra-long Cycle Fatigue of High-Strength Carbon Steels Part I: Review and Analysis of the Mechanism of Failure, *Mater. Sci. Eng., A*, 2013, **356**, p 227-235
3. T. Sakai, Review and Prospects for Current Studies on Very High Cycle Fatigue of Metallic Materials for Machine Structural Use, *J. Solid Mech. Mater. Eng.*, 2009, **3**, p 425-439
4. X. Li, Effects of Inclusions on Very High Cycle Fatigue Properties of High Strength Steels, *Int. Mater. Rev.*, 2012, **57**, p 92-114
5. C. Bathias, Gigacycle Fatigue of Bearing Steels, *Mater. Sci. Technol.*, 2012, **28**, p 27-33
6. Y. Murakami, Material Defects as the Basis of Fatigue Design, *Int. J. Fatigue*, 2012, **41**, p 2-10
7. K. Shiozawa, L. Lu, and S. Ishihara, S-N Curve Characteristics and Subsurface Crack Initiation Behavior in Ultra-long Life Fatigue of a High Carbon Steel-Chromium Bearing Steel, *Fatigue Fract. Eng. Mater. Struct.*, 2001, **24**, p 781-790
8. Y. Ochi, T. Matsumura, K. Masaki, and S. Yoshida, High Cycle Rotating Bending Fatigue Property in Very Long-life Regime of High-cycle Strength Steels, *Fatigue Fract. Eng. Mater. Struct.*, 2002, **25**, p 823-830
9. K. Shiozawa, Y. Morii, S. Nishino, and L. Lu, Subsurface Crack Initiation and Propagation Mechanism in High-Strength Steel in a Very High Cycle Fatigue Regime, *Int. J. Fatigue*, 2006, **28**, p 1521-1532
10. M. Nakajima, N. Kamiya, H. Itoga, K. Tokaji, and H. Ko, Experimental Estimation of Crack Initiation Lives and Fatigue Limit in Subsurface Fracture of High Carbon Steel, *Int. J. Fatigue*, 2006, **28**, p 1540-1546
11. Z. Huang, D. Wagner, Q. Wang, and C. Bathias, Effect of Carburizing Treatment on the "Fish Eye" Crack Growth for a Low Alloyed Chromium Steel in Very High Cycle Fatigue, *Mater. Sci. Eng., A*, 2013, **559**, p 790-797
12. Y. Murakami, T. Nomoto, T. Ueda, and Y. Murakami, On the Mechanism of Fatigue Failure in the Superlong Life Regime ($N > 10^7$ Cycles). Part I: Influence of Hydrogen Trapped by Inclusions, *Fatigue Fract. Eng. Mater. Struct.*, 2000, **23**, p 893-902
13. K. Funatani and F. Noda, The Influence of Residual Stress on the Fatigue Strength of Carburized Hardened Steel, *J. Soc. Mater. Sci. Jpn.*, 1968, **17**, p 1124-1128
14. T. Naito, H. Udea, and M. Kikuchi, Fatigue Behavior of Carburized Steel with Internal Oxides and Nonmartensitic Microstructure near the Surface, *Metall. Trans. A*, 1984, **15A**, p 1431-1436
15. Y. Murakami, T. Nomoto, and T. Ueda, Factors Influencing the Mechanism of Superlong Fatigue Failure in Steels, *Fatigue Fract. Eng. Mater. Struct.*, 1999, **22**, p 581-590
16. Z. Huang, W. Du, D. Wagner, and C. Bathias, Relation Between the Mechanical Behavior of a High Strength Steel and the Microstructure in Gigacycle Fatigue, *Mater. Sci. Forum*, 2010, **636-637**, p 1459-1466
17. "Standard Test Method for Determining Average Grain Size," E112, *Annual Book of ASTM Standards*, vol. 3.01, ASTM, 2012
18. "Standard Test Method for Knoop and Vickers Hardness of Materials," E394, *Annual Book of ASTM Standards*, vol. 3.01, ASTM, 2011
19. M. Moore and W. Evans, Mathematical Corrections for Stress in Removed Layers in X-ray Diffraction Residual Stress Analysis, *SAE Trans.*, 1958, **66**, p 340-345
20. G. Parrish, *Carburizing: Microstructures and Properties*, ASM International, Materials Park, OH, 1999
21. K. Inoue, H. Sonoda, G. Deng, M. Yamanaka, and M. Kato, Effects of CBN Grinding on the Bending Fatigue Strength of Carburized Gears, *J. Mech. Des.*, 1989, **120**, p 606-611

22. R. Pedersen and S. Rice, *Case Crushing of Carburized and Hardened Gears, Technical Paper 610034*, SAE International, Warrendale, PA, 1961
23. R. McClung, A Literature Survey on the Stability and Significance of Residual Stresses During Fatigue, *Fatigue Fract. Eng. Mater. Struct.*, 2007, **30**, p 173-205
24. S. Nishijima and K. Kanazawa, Stepwise S-N Curve and Fish-Eye Failure in Gigacycle Fatigue, *Fatigue Fract. Eng. Mater. Struct.*, 1999, **22**, p 601-607
25. T. Sakai, Y. Sato, and N. Oguma, Characteristic S-N Properties of High Carbon-Chromium Bearing Steel under Axial Loading in Long Life Fatigue, *Fatigue Fract. Eng. Mater. Struct.*, 2002, **25**, p 765-773
26. Y. Shimatani, K. Shiozawa, T. Nakada, and T. Yoshimoto, Effect of Surface Residual Stress and Inclusion Size on Fatigue Failure Mode of Matrix HSS in Very High Cycle Regime, *Procedia Eng.*, 2010, **2**, p 873-882
27. K. Shiozawa, T. Hasegawa, Y. Kashiwagi, and L. Lu, Very High Cycle Fatigue Properties of a Bearing Steel under Axial Loading Condition, *Int. J. Fatigue*, 2009, **31**, p 880-888
28. G. Qian, Y. Hong, and C. Zhou, Investigation of High Cycle and Very High Cycle Fatigue Behavior for a Structural Steel with Smooth and Notched Specimens, *Eng. Fail. Anal.*, 2010, **17**, p 1517-1525
29. W. Hui, Y. Nie, H. Dong, Y. Weng, and C. Wang, High-Cycle Fatigue Fracture Behavior of Ultrahigh Strength Steels, *J. Mater. Sci. Technol.*, 2008, **24**, p 787-792
30. Z. Lei, A. Zhao, J. Xie, C. Sun, and Y. Hong, Very High Cycle Fatigue of GCr15 Steel with Smooth and Hole Defect Specimens, *Theor. Appl. Mech. Lett.*, 2012, doi:10.1063/2.1203103
31. W. Li, T. Sakai, Q. Li, L. Lu, and P. Wang, Reliability Evaluation on Very High Cycle Fatigue Property of GCr15 Bearing Steel, *Int. J. Fatigue*, 2010, **32**, p 1096-1107
32. K. Tanaka and Y. Akiniwa, Fatigue Crack Propagation Behavior Derived from S-N Data in Very High Cycle Regime, *Fatigue Fract. Eng. Mater. Struct.*, 2002, **25**, p 775-784
33. J. Zhang, K. Shiozawa, T. Lu, W. Li, and W. Zhang, Fatigue Fracture Behavior of Bearing Steel GCr15 in Very High Cycle Regime, *Adv. Mater. Res.*, 2008, **44-46**, p 119-126
34. Y. Hong, Z. Lei, C. Sun, and A. Zhao, Propensities of Crack Interior Initiation and Early Growth for Very-High-Cycle Fatigue of High Strength Steels, *Int. J. Fatigue*, 2013, doi:10.1016/j.ijfatigue.2013.02.023
35. Y. Akiniwa, N. Miyamoto, H. Tsuru, and K. Tanaka, Notch Effect on Fatigue Strength Reduction of Bearing Steel in the Very High Cycle Regime, *Int. J. Fatigue*, 2006, **28**, p 1555-1565
36. C. Sun, J. Xie, A. Zhao, Z. Lei, and Y. Hong, A Cumulative Damage Model for Fatigue Life Estimation of High-Strength Steels in High-Cycle and Very-High-Cycle Fatigue, *Fatigue Fract. Eng. Mater. Struct.*, 2012, **35**, p 638-647
37. Y. Liu, Z. Yang, Y. Li, S. Chen, S. Li, W. Hui, and Y. Weng, On the Formation of GBF of High-Strength Steel in the Very High Cycle Fatigue Regime, *Mater. Sci. Eng., A*, 2008, **497**, p 408-415
38. T. Otsuka, H. Hanada, H. Nakashima, K. Sakamoto, M. Hayakawa, K. Hashizume, and M. Sugisaki, Observation of Hydrogen Distribution around Non-Metallic Inclusions in Steels with Tritium Microautoradiography, *Fusion Sci. Technol.*, 2005, **48**, p 708-711
39. K. Shiozawa and L. Lu, Internal Fatigue Failure Mechanism of High Strength Steels in Gigacycle Regime, *Key Eng. Mater.*, 2008, **378-379**, p 65-80
40. P. Novak, R. Yuan, B. Somerday, P. Sofronis, R. Ritchie, and A. Statistical, Physical-based, Micro-Mechanical Model of Hydrogen-Induced Intergranular Fracture of Steel, *J. Mech. Phys. Solids*, 2010, **58**, p 206-228
41. P. Grad, B. Reuscher, A. Brodyanski, M. Kopnarski, and E. Kerscher, Mechanisms of Fatigue Crack Initiation and Propagation in the Very High Cycle Fatigue Regime of High Strength Steels, *Scr. Mater.*, 2012, **67**, p 838-841
42. H. Streng, C. Razim, and J. Grosch, Diffusion of Hydrogen during Carburization and Tempering, *Heat Treatment and Surface Engineering, New Technology and Practical Applications*, G. Krauss, Ed., ASM International, Chicago, 1988, p 313-317
43. Y. Li, Z. Yang, Y. Liu, S. Li, G. Li, W. Hui, and Y. Weng, The Influence of Hydrogen on Very High Cycle Fatigue Properties of High Strength Spring Steel, *Mater. Sci. Eng., A*, 2008, **489**, p 373-379
44. Y. Li, S. Chen, Y. Liu, Z. Yang, S. Li, W. Hui, and Y. Weng, The Characteristics of Granular-Bright Facet in Hydrogen Pre-Charged and Uncharged High Strength Steels in the Very High Cycle Fatigue Regime, *J. Mater. Sci.*, 2010, **45**, p 831-841
45. Y. Murakami and H. Matsunaga, The Effect of Hydrogen on Fatigue Properties of Steels Used for Fuel Cell System, *Int. J. Fatigue*, 2006, **28**, p 1509-1520